

Interacting Kaons on Nucleons (IKON)

L. Bosisio¹, L. Busso², P.Camerini¹, D. Calvo³, F. De Mori⁴,
A. Filippi³, P.M. Gensini⁵, N. Grion⁶, A. Olin⁷, V. Paticchio⁸,
S. Piano⁶, R. Wheadon³

April 22, 2010

¹Dip. Fisica and INFN, Trieste, Italy

²Dip. Fisica Generale and INFN, Torino, Italy

³INFN Torino, Italy

⁴Dip. Fisica Sperimentale and INFN, Torino, Italy

⁵Dip. Fisica and INFN, Perugia, Italy

⁶INFN Trieste, Italy

⁷TRIUMF, Canada

⁸INFN Bari, Italy

Abstract

Physics and motivations for the study of low-energy KN and Kd scattering and reactions are discussed. An experiment to perform such measurements at the DAΦNE collider LNF (Frascati) is proposed and its features sketched.

Contents

1	Introduction and motivations	3
2	The Physics Case	7
2.1	K^+N interaction	8
2.1.1	K^+p scattering, $I = 1$	9
2.1.2	K^+d scattering	10
2.2	$K_L^0 p$ scattering	12
2.3	K^-N interaction	13
2.3.1	K^-p scattering	13
2.3.2	K^-d scattering	16
2.3.3	Baryonic resonances in the $\bar{K}N$ channel	17
3	Expected event counting for selected reactions	22
4	Reaction kinematics and experimental constraints	24
5	The vertex detector (VDET)	27
5.1	VDET, simulations	27
5.2	VDET, hardware	32
5.2.1	Sensor	33
5.2.2	Read-out Electronics	33

Chapter 1

Introduction and motivations

Data on kaon-induced reactions at low energies on nucleons and deuterons, i.e., KN and Kd total and differential cross sections are insufficient for the demand. Below $150 \text{ MeV}/c$, the available data deal only with the $K^\pm p$ interaction and belong to old bubble chamber experiments. In addition, these data are affected by large errors, see Fig. 1.1. This situation becomes even worse when considering the $K^\pm n$ and $K^\pm d$ interactions since no data exist for momenta below $500 \text{ MeV}/c$.

DAΦNE is nowadays the only world facility where low-energy KN and Kd experimental studies can be pursued. In fact, the nearly at-rest decay of the $\phi(1020)$ meson produced in e^+e^- collisions, $\phi(1020) \rightarrow K^+K^-$ (B.R. 50%), delivers charged kaons with momenta in the $(110 \div 140) \text{ MeV}/c$ momentum range, see the dashed stripe in Fig. 1.1 [1]. Pairs of K^+K^- 's, being tracked until the target volume, account for an almost monochromatic and clean *beam*. The DAΦNE crab configuration ensures about $10^3 K^\pm/s$, which will allow the proposed studies to be performed in about 1.5 years of beam-time. By exploiting these unique features of the DAΦNE K^\pm -beam, a thoroughly unexplored research field becomes available to studies of elementary scattering and reactions involving strangeness. Some observables of these reactions can be related to chiral symmetry breaking effects as well as to the excitation of baryonic resonances close to threshold.

To this end, the K^\pm tracks must initially be reconstructed up to their interaction point into the target (Hydrogen or Deuterium) and final state particles be identified and analyzed. The K^\pm tracking will be provided by a segmented and thin detector (VDET) based on silicon technology, while final state particles (either charged or neutral) will be measured by combining the VDET with KLOE information. The use of gaseous or thin solid targets of different composition also opens a window to the study of the $K^\pm A$ interaction, which offers the possibility of investigating regeneration phenomena

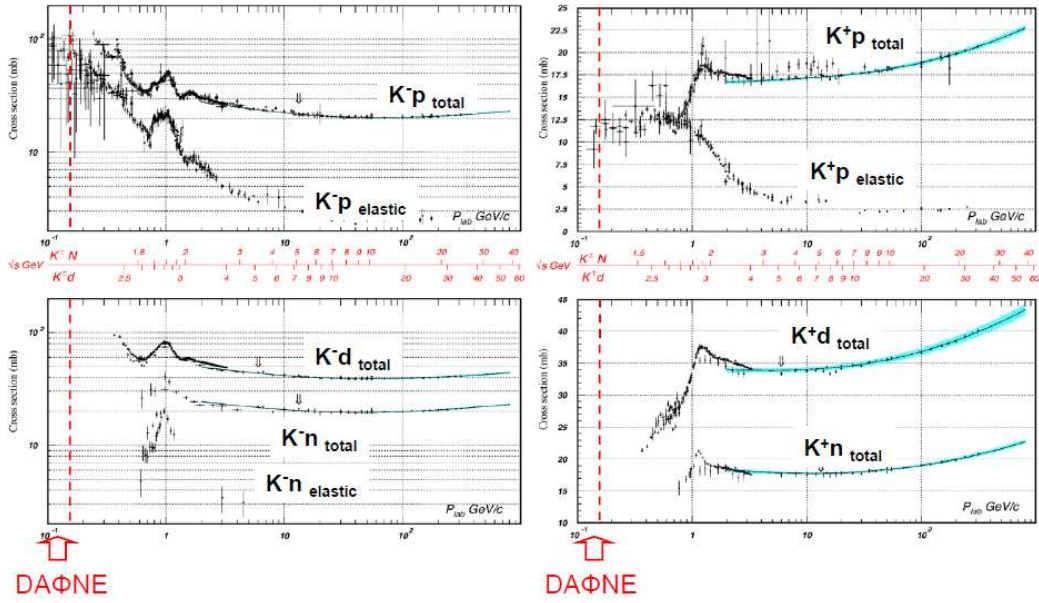


Figure 1.1: Cross sections of K^- and K^+ induced reactions on protons, neutrons and deuterons.

involving K_L^0 and K_S^0 in matter.

The ambition of the proposed experiment is to provide a systematic study of cross sections induced by low-energy kaons on nucleons and deuterons. This would prompt further theoretical searches as well as advanced calculations which cannot presently be performed because of the poor quality or unavailability of data.

The elementary reactions to be studied are the elastic and inelastic scattering off protons, neutrons and deuterons. They are listed below:

1. K^\pm elastic scattering on protons: $K^-p \rightarrow K^-p$, $K^+p \rightarrow K^+p$;
2. K^\pm elastic scattering on neutrons. This study requires a Deuterium target: $K^-d \rightarrow K^-np$, $K^+d \rightarrow K^+np$;
3. K^\pm elastic scattering on deuterons: $K^-d \rightarrow K^-d$, $K^+d \rightarrow K^+d$;
4. charge exchange reactions: $K^-p \rightarrow \overline{K}^0n$, $K_L^0p \rightarrow K^+n$ (threshold: $p_{K^-} = 89 \text{ MeV}/c$);
5. regeneration reaction: $K_L^0p \rightarrow K_S^0p$;
6. inelastic K^- interactions on protons close to threshold:
 - (a) $K^-p \rightarrow \Lambda\pi^0$;

- (b) $K^-p \rightarrow \Sigma^\pm \pi^\mp$;
- (c) $K^-p \rightarrow \Sigma^0 \pi^0$

7. inelastic K^- interactions on deuterons close to threshold: $K^-d \rightarrow \pi Y N$
($Y = \Lambda, \Sigma$);

For the above reactions, the aim is to measure both total and differential cross sections for at least two different momenta below 120 MeV/ c .

The kaon radiative capture is another class of inelastic processes which might be studied at DAΦNE. For a Hydrogen target, the reactions to be studied are $K^-p \rightarrow \gamma \Lambda(\Sigma^0)$. When using a Deuterium target, the kaon radiative capture can also be examined on neutrons by means of the reactions $K^-d \rightarrow \gamma \Sigma^- p$ and $K^-d \rightarrow \gamma \Sigma^0(\Lambda)p$. Up to now, these processes were investigated by simply detecting photons following kaon captures. But experiments did not succeed disentangling photons from radiative capture or π^0, Σ^0 decays. Therefore, only rough estimates of the reaction branching ratios exist. A large acceptance apparatus ($\sim 4\pi$) and highly efficient to photon detection (KLOE) should make possible the complete identification of the reaction final states; therefore, the determination of the absolute cross sections of these largely unknown processes.

The quest for more precise (especially for anti-) kaon scattering data is nowadays triggered by the existence of inconsistencies in the low energy kaon interactions data. The new measurements by DEAR of the strong interaction shift and width of the kaonic atom and the K^-p scattering length [2] are in disagreement with both earlier measurements [3] and the existing kaon scattering database; therefore, a comprehensive description of the $KN(A)$ interaction based on the today available measurements is not possible [4, 5, 6, 7, 8]. Such an inconsistency calls for new kaonic atom measurements being able of affirming (denying) the DEAR measurement; to this purpose, the SIDDHARTA experiment is currently running at LNF.

In the past, a number of models were developed to describe the low-energy KN interaction, which are based on SU(3) chiral Lagrangian with coupled channels [9, 11, 12]. However, they are necessarily approximated because of the presence of several resonances in the $\bar{K}N$ system, which prevent the application of a perturbative treatment. The model predictions would be strengthened by quality close-to-threshold scattering data. In addition, the sub-threshold behavior of the $\bar{K}N$ interaction (ex., sub-threshold resonances) cannot experimentally be accessed, it can only be predicted by models; however, they are primarily requested to fit the over-threshold experimental data.

The quality (and quantity) of close-to-threshold KN data is a key issue for theoretical research since it constrains the range of validity of theories.

The information provided by the K scattering on Hydrogen will have an immediate feedback since it can be directly inserted in all the KN calculations. The scattering on Deuterium implies a rather complex three-body problem, which calls for the application of few-body techniques and opens new scenarios to theoretical investigations. The KN interaction field raised considerable interest at the time the DAΦNE project was presented and developed [13] but, up to now, experiments aiming at low-energy $KN(d)$ studies have never been pursued [14]. Based on the KA knowledge achieved with FINUDA, we propose a new initiative aimed at studying the low-energy $KN(d)$ interactions which, we believe, will complete the FINUDA physics program.

Chapter 2

The Physics Case

The K^+ and K^- behavior in a scattering process is very different and markedly depends on the meson strangeness content. For low-energy K^+ 's only elastic and charge exchange reactions can occur. The strength of the K^+ interaction with nucleons is rather modest and varies slowly with energy. The behavior of K^+N scattering can be described by a thorough perturbative approach, which yields direct knowledge of some parameters of SU(3) chiral perturbation theories and the strangeness content of the nucleon (through the Sigma-term evaluation). Since the interaction of positive kaons with hadrons is rather mild, they can be used as probes to test and study the single particle nuclear density (especially) of neutrons in nuclei. For K^- 's, the presence of the \bar{u} quark opens a wider variety of processes to the interacting kaon, being now allowed the formation of $I = 0, 1$ resonances; for example, $\Sigma^*(1385)P_{13}$, $\Lambda(1405)S_{01}$, $\Lambda(1520)D_{03}$ and $\Sigma(1660)P_{11}$. The excitation of these resonances prevents a perturbative treatment from being used when describing the $\bar{K}N$ interaction dynamics. Therefore, only approximate multichannel-coupled models can be formulated whose degree of precision must be tested against the experimental data. For some of these resonances, the close-to-threshold $\Lambda(1405)$ and $\Sigma^*(1385)$, the formation mechanism is still unclear and their understanding calls for state-of-the-art theoretical calculations [15, 16, 17, 18, 19].

The interaction of kaons with a few-nucleon system is documented by few articles: there are low-statistics data taken with bubble chambers [20], and only recently the FINUDA collaboration has published data describing the K^- absorption at rest in light nuclei with the emission of correlated Λp , Λd and Λt pairs [21, 22, 23], and the K^+ charge-exchange reaction on ${}^6\text{Li}$ [24].

2.1 K^+N interaction

This section presents a summary of the main experimental outcomes of the KN reaction. A thorough review can be found in Ref. [25].

The $I = 1$ part of the KN scattering amplitude can thoroughly be studied with the K^+p reaction (Hydrogen target). The upper left part of Fig. 2.1 shows the trend of the K^+p ($I = 1$) elastic and total cross sections as a function of the kaon momentum. Both have flat behavior below 800 MeV/c, and most of the reaction strength belongs to the K^+p elastic scattering.

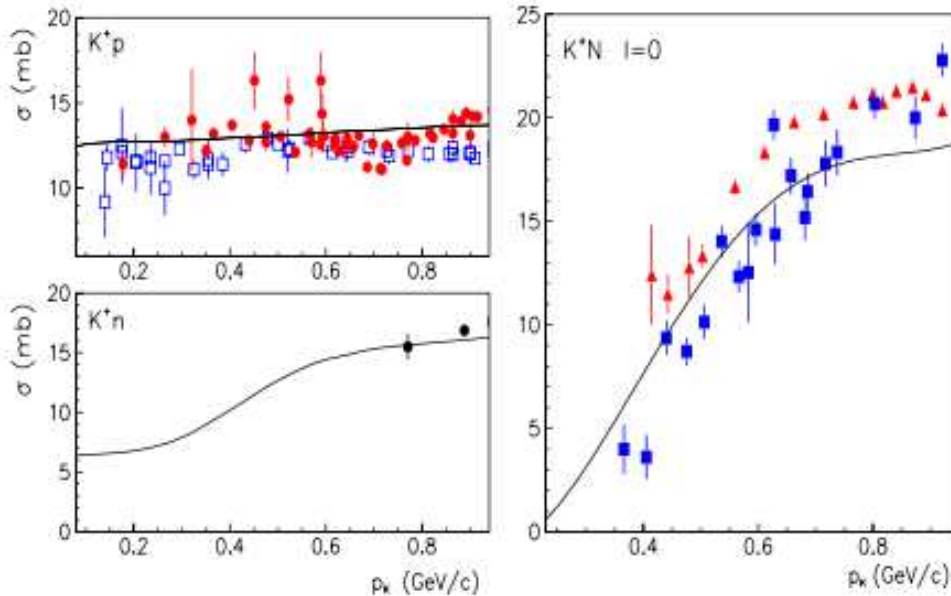


Figure 2.1: Cross sections of the K^+p and K^+n elastic reactions. Upper left: K^+p ($I = 1$) elastic (open squares, from Ref. [26]) and total (red full circles, from Ref. [26]) cross sections. Lower left: K^+n total cross section (full black circles, from Ref. [26]). Right: K^+N ($I = 0$) cross section (red triangles, data from Ref. [28] and blue squares, data from [27]). The continuous lines are the results of the Jülich (KN) model [29]. The figures are taken from Ref. [30].

The $I = 0$ part of the amplitude can be studied by using a Deuterium target, or by means of neutral kaon charge-exchange reactions. In general, the $K^+d \rightarrow K^+pn$ break-up reaction is not studied accurately since the existing measurements failed to identify the hit proton or neutron; therefore, they could not reliably define the isospin value of the reaction initial state. The available K^+n measurements yield a total and an extracted KN ($I = 0$) cross

sections which are shown in Fig. 2.1. At a rough estimate, $\sigma_{K^+p} \sim 2\sigma_{K^+n}$ at low momenta.

2.1.1 K^+p scattering, $I = 1$

In the momentum range from 145 to 2000 MeV/ c , the K^+p elastic scattering database is the most populated set of data. At low momenta, this channel is not affected by the π production process since it opens at 525 MeV/ c . Below 130 MeV/ c , the K^+p elastic reaction dominantly occurs in s -wave, p -wave contributions can therefore be neglected. At around 100 MeV/ c , the total cross section for $K^+p \rightarrow K^+p$ is of the order of 10 mb [1].

At low momenta the Coulomb interaction heavily interferes with the nuclear scattering process thus playing an important role. Its contribution dominates at forward angles ($\theta_{lab} \leq 10^\circ$), so it can be easily identified and separated. The interference between the Coulomb and the nuclear scattering amplitudes makes possible to derive the sign and magnitude of the kaon scattering length. The available data allow the kaon scattering length to be determined with an accuracy better than 10% [32]. A measurement of K^+p differential cross sections at low energy and forward angles will further improve the precision of the K^+p scattering length determination of about one order of magnitude [33].

Determination of the KN Sigma-terms

Meson-baryon scattering data can be used to calculate Sigma-terms, which are correlated to the particle quark content. In SU(3) based theories, Sigma-terms can be used to obtain information on the explicit breaking of the chiral symmetry and to study the strange-quark content of the baryon involved in the interaction. Many efforts were made to extract the Sigma-term value from the πN scattering [34]. Sigma-terms can also be defined for the KN scattering [35]; the method to extract them relies on the analytic continuation of the KN scattering amplitude by means of dispersion relations. However, the KN database is meager and this prevents a reliable determination of the KN Sigma-terms [36].

The two isospin states of the KN interaction in the t -channel, $I = 0, 1$, define two Sigma-terms [35]. The $\Sigma_{KN}^{I=0}$ -term is the relevant observable to be considered for extracting the strangeness content of the nucleon. An assessment of $\Sigma_{KN}^{I=0}$ was made several years ago [37], which bears huge errors because of the poor world KN database. Other estimations were recently made, which were based on Next-to-leading order heavy baryon chiral perturbation theory [14, 33], but again they result being affected by large un-

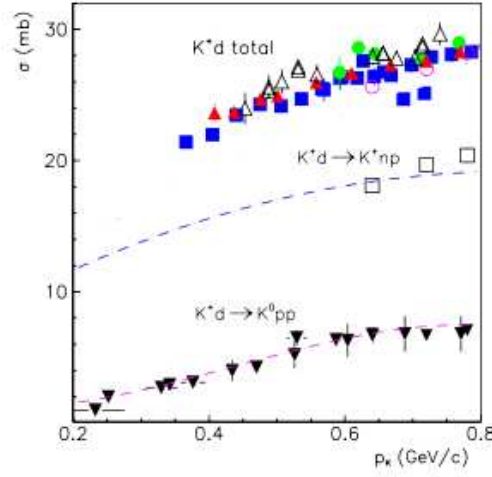


Figure 2.2: Total K^+d , and integrated $K^+d \rightarrow K^+pn$ and $K^+d \rightarrow K^0pp$ cross sections. The experimental points are from the following papers: blue squares, Ref. [27]; red triangles, Ref. [28]; green circles, Ref. [38]; open triangles, Ref. [39]; open circles and open squares, Ref. [40]; black triangles, Ref. [41, 42]. The continuous lines are the results of the Jülich (KN) model [29]. The figure is taken from Ref. [30].

certainties. The size of the kaon mass requires the inclusion of higher order terms in the calculations, which so far were not considered because of the poor quality of the KN database. The availability of quality KN differential cross sections will prompt new calculations. As an example, if the K^+p cross sections were measured with a precision of 10%, the resulting $\Delta\Sigma_{KN}^{I=0}$ would be $\sim 0.05 m_K$, $0.2 m_K$ being the world present limit.

2.1.2 K^+d scattering

Fig. 2.2 shows the K^+d total cross section, which is the sum of the cross sections of the KN elementary processes occurring in deuteron (Deuterium target), i.e., the break-up (or quasi-elastic) reaction $K^+d \rightarrow K^+pn$, charge-exchange reaction $K^+d \rightarrow K^0pp$ and coherent scattering $K^+d \rightarrow K^+d$. In the following some features of each of these reactions will be presented.

Break-up reaction, $K^+d \rightarrow K^+pn$

Data on the $K^+d \rightarrow K^+pn$ reaction are available for kaon momenta from 342 MeV/c onwards. Previous measurements failed to detect the recoiling

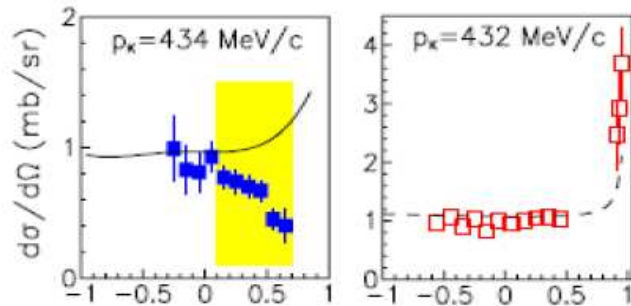


Figure 2.3: $K^+p \rightarrow K^+p$ differential cross section as a function of the kaon scattering angle in the center-of-mass system, for two close values of the K^+ incident momentum. The filled squares show the results extracted from the $K^+d \rightarrow K^+pn$ reaction with a reconstructed neutron spectator [41]. The yellow area indicates the angular range where the data analysis was considered to be ambiguous. The open squares are the differential cross sections measured on a hydrogen target [31]. The solid lines shows the calculations made in the framework of the Jülich model [29].

nucleon (either proton or neutron), which is the basic problem in the study of this reaction. In these experiments, the recoiling nucleon was treated as a *spectator* and its vector momentum was indirectly deduced from the energy balance of the reaction. Such an approximation however is too coarse for a correct description of the interaction. This is also evident in the experimental data: Fig. 2.3 compares the differential cross sections of the reactions $K^+d \rightarrow K^+p(n_s)$ and $K^+p \rightarrow K^+p$, where the notation n_s indicates the neutron spectator. The difference in shape and intensities cannot simply be explained by the small binding energy of n_s nor by the reaction mechanism being involved a single nucleon.

The interaction of a kaon with a deuteron is a genuine three-body problem, which must be treated by few-body techniques (i.e., Faddeev integral equations), taking into account the Fermi motion of the interacting nucleon and the three-body kinematics of the final state. Some approximate models were proposed to describe the KN reaction in a deuteron; as an example, a KN model based on meson and baryon exchange (such as the Jülich model [29]) was combined with a single-scattering impulse approximation (for the description of the recoiling nucleon) [30]. In spite of the approximations, the model predictions (dashed lines in Fig. 2.2) are capable of describing the few $K^+d \rightarrow K^+pn$ integrated cross section data. It is also worth mentioning that this model describes reasonably well the K^+N ($I = 0$) cross sections (see discussion in section 2.1, K^+N interaction, and Fig. 2.1) whose values

are extracted from K^+d cross section by applying the high-energy Glauber formalism [43]. However, such a formalism is itself a source of uncertainty which further affects the quality of the data set.

All these observations call for exclusive (and accurate) measurements. At the present state-of-the-art, the break-up reaction measurements are practically useless as inputs for understanding the KN interaction.

Charge Exchange, $K^+d \rightarrow K^0pp$

The model mentioned in the last subsection describes fairly well the differential cross sections of the $K^+d \rightarrow K^0pp$ charge-exchange reaction. These data are more precise than the elastic or quasi-elastic K^+d scattering data. The trend of the angle-integrated cross section is shown in Fig. 2.2, the dashed line results from the model of Ref. [30]. The charge exchange reaction cross section at $p_K = 252$ MeV/ c is the lowest energy measurement available for the K^+d interaction.

Coherent (elastic) scattering, $K^+d \rightarrow K^+d$

Fig. 2.4 shows the trend of the coherent K^+d scattering as a function of the incident kaon momentum. The interaction is dominated by the p -wave amplitude above 300 MeV/ c . The angular distributions (not shown) indicate that this reaction goes mainly through the $I = 1$ component of the K^+N scattering amplitude. The differential cross sections are in good agreement with the Jülich model at forward angles but it fails to predict the differential cross section at backward angles. This part of the differential cross section seems to be driven by multiple scattering effects, which are not accounted for by the Jülich model.

2.2 $K_L^0 p$ scattering

No data for neutral kaon scattering exist below 500 MeV/ c , and the existing data at higher momenta bear error bars as high as a $\sim 20\%$. Measurements of the $K_L^0 p \rightarrow K^+n$ cross section can sizably be improved (if compared with regeneration measurements) because of the KLOE capability of tagging K_S^0 's. In this case, the K_L^0 counting is ensured by KLOE via the $K_S^0 \rightarrow \pi^+\pi^-$ decay measurement while K^+ 's are detected by VDET. Therefore, a reasonable efficiency of KLOE to low-energy neutrons would allow an accurate measurement of the $K_L^0 p \rightarrow K^+n$ reaction. This measurement represents a unique input for the precise determination of the $I = 0$ amplitude of the KN scattering.

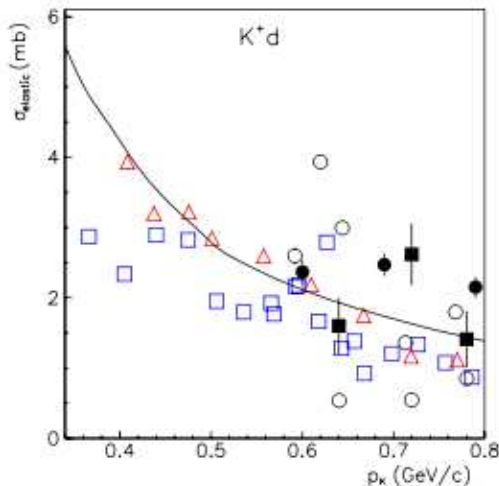


Figure 2.4: Angle-integrated cross section of the $K^+d \rightarrow K^+d$ coherent reaction. Full markers, experimental points from Refs. [44, 45, 46]. Open markers, data derived from indirect measurements Ref. [30]. The solid line is the result of the Jülich (KN) model [29]. The figure is taken from Ref. [30].

2.3 K^-N interaction

2.3.1 K^-p scattering

Several theoretical models based on chiral $SU(3)$ describe the dynamics of the $\bar{K}N$ interaction by using the complete experimental database [4, 5, 6, 7]. The models mainly differ for the number of terms added to the first order interaction (contact, Tomozawa-Weinberg) and the inclusion of interference effects such as the Coulombian one. All the models are based on a chiral effective Lagrangian, which describes the coupling of the pseudo-scalar meson octet (π, K, η) to the ground state baryon octet (N, Λ, Σ, Ξ) following the basic approach proposed in Refs. [9, 11]. Moreover, a coupled-channel approach must be adopted to achieve a reasonable description of the data.

The input data for these models include scattering cross sections, the shift and width of kaonic Hydrogen (so far provided by the DEAR [2] and KEK KpX [3] measurements), the line-shape of $\Sigma\pi$ invariant mass spectra and the close-to-threshold K^-p hadronic branching ratios. The latter were measured rather precisely [10] and are defined as:

$$\begin{aligned} \gamma &= \Gamma(K^-p \rightarrow \Sigma^+\pi^-)/\Gamma(K^-p \rightarrow \Sigma^-\pi^+) = 2.36 \pm 0.04, \\ R_c &= \Gamma(K^-p \rightarrow \text{charged particles})/\Gamma(K^-p \rightarrow \text{all}) = 0.664 \pm 0.011, \end{aligned}$$

$$R_n = \Gamma(K^-p \rightarrow \pi^0\Lambda)/\Gamma(K^-p \rightarrow \text{all neutral states}) = 0.189 \pm 0.015.$$

Tests of model response to different KN data sets clearly point out systematic discrepancies among data sets supplied by different measurements. These discrepancies are independent of the theoretical framework used, either be chiral based [7] or be a few-body approach [8]. The critical data set is the newest kaonic-atom measurement [2], which is at odds with previous kaonic-atom data and with the whole remainder of the \overline{KN} database. This clearly calls for new and precise input data.

A summary of the available measured K^-p cross sections for several reactions is given in Figs. 2.5 throughout 2.8. The blue band is an example of the confidence region of one of the theoretical approaches currently used to describe the \overline{KN} data [6]. The continuous line represents the data best fit. The band-width depends on the approach used; however, it is evident that the model calculations satisfactorily fit the high-momentum region but fail to reproduce the low-momentum region, since there are just few available data.

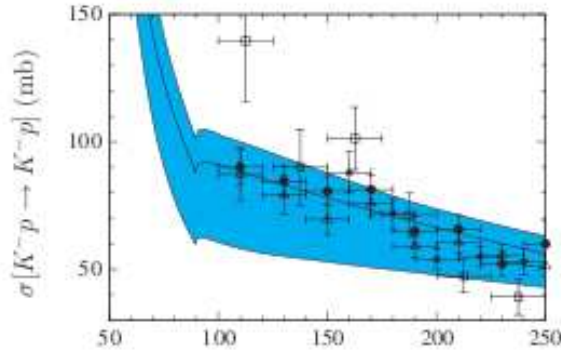


Figure 2.5: K^-p elastic cross section, experimental data are from Ref. [47] (open squares), [46] (open triangles), [48] (full circles). The curves are from Ref. [6].

Fig. 2.5 shows the trend of the elastic K^-p cross section, which has the most wealthy and precise database among the K^-N reactions [47, 46, 48]. The cross section drops monotonically with the kaon incident momentum, until the opening of the $\Lambda(1520)$ resonance (not shown in the figure). The models are able to describe the data down to 100 MeV/ c . At the opening of the $\overline{K^0}n$ channel cusps are visible as a consequence of the coupled-channel approach. At around 100 MeV/ c the total cross section is about 80 mb.

The $K^-p \rightarrow \overline{K^0}n$ charge-exchange behavior [47, 48, 49, 50, 51] can roughly be reproduced by the models, see Fig. 2.6. For this channel, the

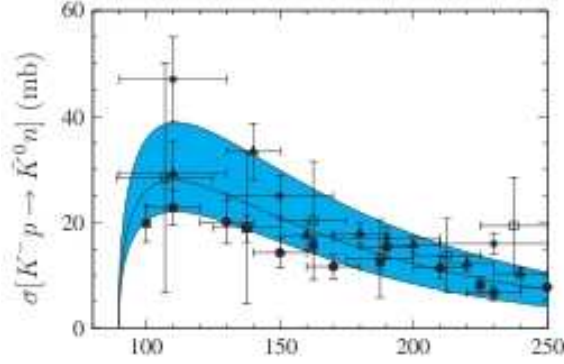


Figure 2.6: $K^-p \rightarrow \overline{K}^0 n$ (CEX) cross section from Ref. [47] (open squares), [48] (full circles), [49] (full squares), [50] (stars), [51] (full triangles). The curves are the result of coupled-channel models [6].

total cross section is ~ 20 mb at ~ 100 MeV/ c .

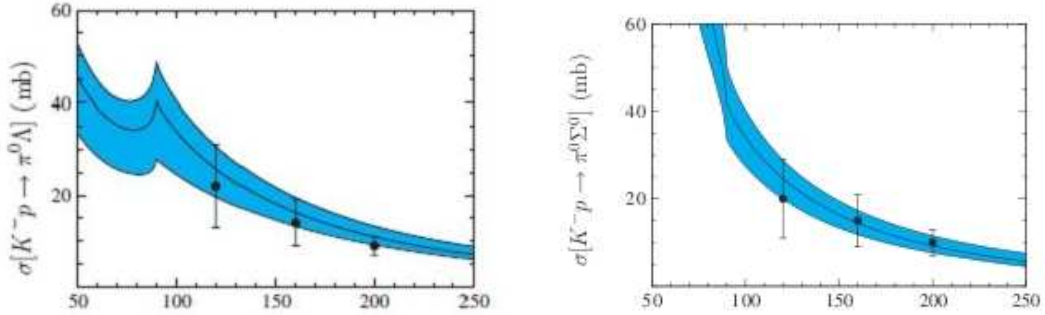


Figure 2.7: Cross sections for the reactions $K^-p \rightarrow \Lambda\pi^0$ (left) and $K^-p \rightarrow \Sigma^0\pi^0$. Data are from Ref. [48]. The curves belong to coupled-channel models and are taken from Ref. [6].

For the $\Lambda\pi^0$ and $\Sigma^0\pi^0$ channels (see Fig. 2.7), the measurements are hardly any [48], which basically prevents models to be tested. By extrapolating the model predictions, the total cross section at 100 MeV/ c is about 40 mb and 20 mb for the $\Lambda\pi^0$ and $\Sigma^0\pi^0$ channels, respectively.

The data for the $\Sigma^\pm\pi^\mp$ channels are precise and rather abundant [47, 46, 48]. The $\Sigma^-\pi^+$ cross section, shown in Fig. 2.8 (left), is satisfactorily reproduced by the model of Ref. [6] despite the large error bars at low momenta. This reaction channel has a total cross section of about 50 mb at 100 MeV/ c . The $\Sigma^+\pi^-$ data are shown in Fig. 2.8 (right), which appear sparse and affected by larger errors. The theoretical models are capable of

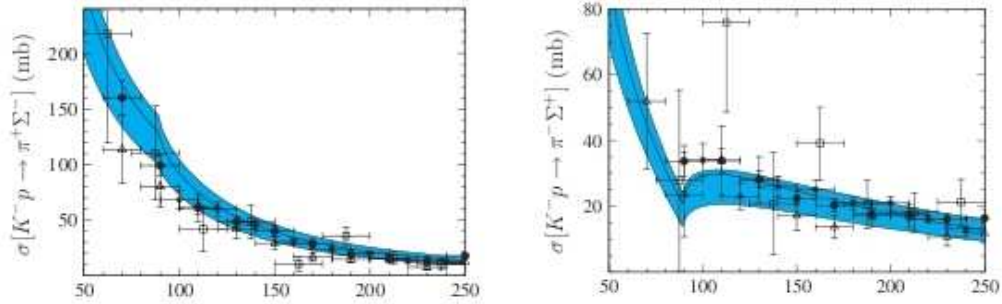


Figure 2.8: $K^-p \rightarrow \Sigma^- \pi^+$ (left) and $K^-p \rightarrow \Sigma^+ \pi^-$ cross sections. Data are taken from Refs. [47] (open squares), [46] (open triangles), [48] (full circles), while the curves are based on coupled-channel models [6].

predicting the cross section, which at 100 MeV/c is about 35 mb.

2.3.2 K^-d scattering

The K^-d scattering data are useful to describe the $I = 1$ part of the $\overline{K}N$ interaction. These data basically suffer the same problem as described for the K^+n reaction, namely, the ambiguity in the determination of the hit nucleon. For the existing measurements, mainly performed in the Seventies and Eighties, the cross section determination was based on the impulse approximation. Such an approximation assumes that the incident particles interacts with one nucleon of the deuteron, while the second is considered to be a *spectator*, its momentum distribution being described by the Hulthén wave function [52]. Within this hypothesis, the K^-n reactions could reasonably be identified by measuring the low-momentum proton or by assuming a missing proton in the final state if its momentum was below 80 MeV/c. Finally, for the inelastic reactions the situation is more favorable as the difference in momenta of the nucleons in the final state is generally large, and the effective reaction can be easily identified.

The K^-d interaction offers a variety of accessible final states, which involves the break-up reaction $\overline{K}NN$ as well as the inelastic reaction channels $\pi\Lambda N$ and $\pi\Sigma N$. The description of the complete phenomenology of the K^-d interaction is a demanding task since the opening of resonances prevents approximate calculations from being developed. In addition, many inelastic reactions can occur on only two (or more) bodies; therefore, the K^-d elementary interactions can be used as input to understand the dynamics of reactions on heavier nuclei.

In the present survey, a thorough study of the $K^-d \rightarrow YN$ reactions is

proposed in order to augment the cross section database, which is insufficient (and old) for the demand. The $K^-d \rightarrow \pi YN$ reactions will also be studied, which deliver important information on some YN interaction features. In addition, the appearance of ΛN and ΣN unconventional resonances [53] will carefully be examined. The πY interaction is another topic whose study is accessible via the $K^-d \rightarrow \pi YN$ reaction. The only information available on $Y\pi$ comes from the $\bar{K}N \rightarrow Y\pi$ reaction; however, the region below this reaction threshold cannot be accessed, and above it the existing data are still scarce.

Measurements of the $K^-d \rightarrow YN$ reaction are dated. They deal with the K^-d interaction at rest [54] and in-flight $K^-d \rightarrow \pi^- \Lambda p$ at incident momenta above 400 MeV/c [55, 56]. This channel featured a structure in the (Λp) invariant mass close to the ΣN threshold (see the peak-structure at ~ 3130 MeV in Fig. 2.9). The structure was later explained as being a dynamical cusp emerging from the opening of the ΣN coupled channel. This observation is very interesting since recently a similar structure was detected in the same (Λp) mass region by K^- absorption measurements in ^4He [57], ^6Li [58] and

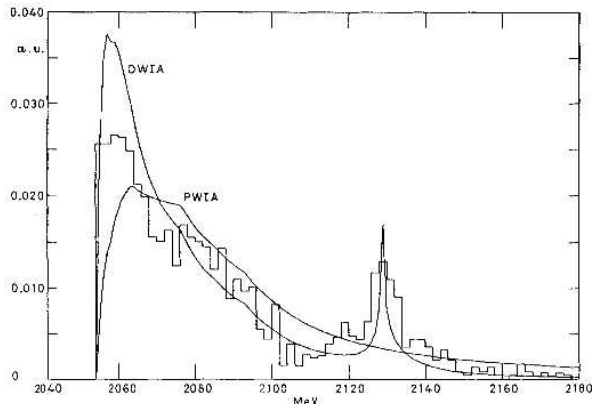


Figure 2.9: Invariant mass of the (Λp) system in the $K^-d \rightarrow \pi^- \Lambda p$ reaction at 700 MeV/c, data are from Ref. [55]. The curves are the result of the Partial (PWIA) and Distorted Wave Impulse Approximation calculations [53].

in heavy ion scattering [59]. A new high statistics experiment measuring the $K^-d \rightarrow \pi^- \Lambda p$ reaction improves the precision of the cusp description, thus allowing a similar effect to be studied in deuterium.

2.3.3 Baryonic resonances in the $\bar{K}N$ channel

In the study of the $\bar{K}N$ interaction at low energy, an open riddle is the under-threshold S -wave $\Lambda(1405)$ baryon [60]. Its nature is still controversial

since data describing the $\Lambda(1405)$ shape are encumbered by large error bars. Recent experiments however delivered novel results, which are now under scrutiny [61, 62].

According to recent theoretical studies, the $\Lambda(1405)$ baryon can be accounted for by the superimposition of two poles emerging from the dynamical interaction between a $\bar{K}N$ system and the $Y\pi, \bar{K}N, Y\eta$ coupled channels [15, 16, 17]. The position and nature of the poles depend on the model ansatz; however, the first pole at 1420 MeV/ c^2 is mostly coupled to $\bar{K}N$ while the second pole, of smaller mass, is associated with the $\Sigma\pi$ channel. Fig. 2.10 reports a collection of solutions from different models, which yield the pole positions for the $\Lambda(1405)$ formation in the complex energy plane. The red and the blue points outline the $\bar{K}N$ -coupled and $\Sigma\pi$ -coupled pole positions, respectively. In this framework, the open points belong to calculations not using a coupled-channel analysis [63] while the full points show the two pole positions for a coupled-channel approach (see figure caption for more details). It can be noticed that the spread of the pole positions among different models is rather wide.

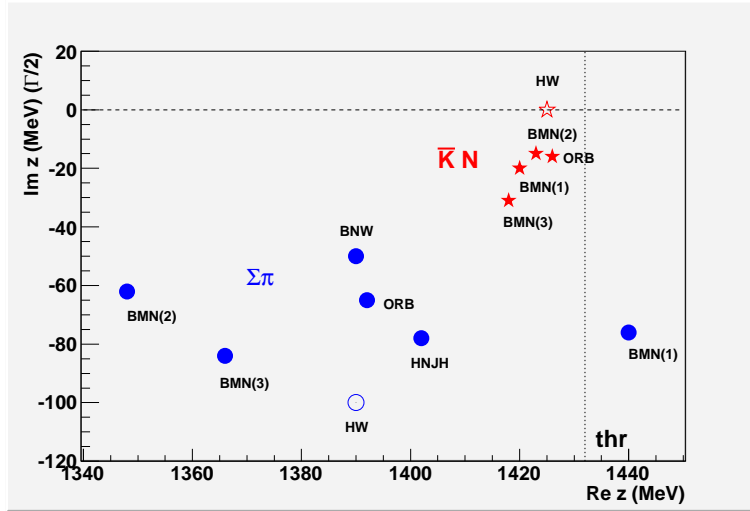


Figure 2.10: $\Lambda(1405)$ poles positions in the complex energy plane according to different theoretical approaches. The red markers correspond to the pole coupled to the $\bar{K}N$ channel while the blue ones to the pole coupled to the $\Sigma\pi$ channel. The open markers refer to a single-pole analysis, the full ones to analyzes with coupled channels. The values are extracted from the following papers: HW Ref. [63], ORB Ref. [64], BMN Ref. [6], BNW Ref. [4], HNJJ Ref. [65].

The features of the $\Lambda(1405)$ baryon can be inferred by measuring the

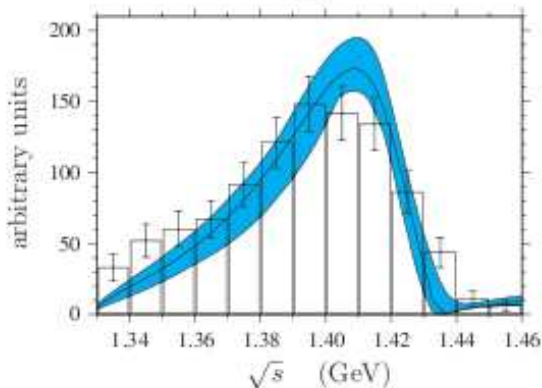


Figure 2.11: $\Sigma^+\pi^-$ invariant mass spectrum from Ref. [67]. The curves are from coupled channel models, Ref. [6].

$\Lambda(1405) \rightarrow \Sigma\pi$ decay [66, 67]. A model calculation capable of providing a comprehensive description of the $\bar{K}N$ interaction (i.e., kaon scattering and kaon atoms) should also be capable of predicting the line-shape of the $\Sigma\pi$ invariant mass [6]. As an example, Fig. 2.11 shows the $\Sigma^+\pi^-$ resonance line-shape [67, 68] being predicted by one of the possible models (namely, the simplest order approximation). The blue band shows the range of variability of the model [6] and the curve the best fit to the data. The (best to-date) description is not satisfactory; however, the picture improves when more terms are added to the effective Lagrangian but the available database is still too meager to successfully constrain the model parameters.

The observation of a mass pole coupled to the $\bar{K}N$ channel requires either an in-flight kaon interaction or kaons being absorbed by a many-body system. So, a $\Lambda(1405)$ survey can only be performed via indirect measurement of reactions such as $\gamma p \rightarrow \Lambda(1405)K^*$, $K^-p \rightarrow \gamma\Lambda(1405)$, $K^-p \rightarrow \pi^0\Lambda(1405)$ since the $\Lambda(1405)$ is produced below the $\bar{K}N$ threshold.

A serious problem which arises in the study of such baryons is to separate

	$\Lambda(1405)$	$\Sigma(1385)$
$\Sigma^+\pi^-$	0.33	0.06
$\Sigma^0\pi^0$	0.33	no
$\Sigma^+\pi^-$	0.33	0.06
$\Lambda\pi^0$	no	0.88

Table 2.1: Measured decay branching ratios of $\Lambda(1405)$ and $\Sigma^*(1385)$. Data are taken from [1].

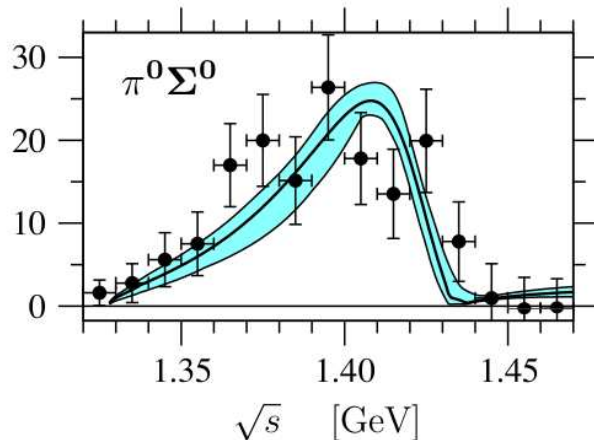


Figure 2.12: $\Sigma^0\pi^0$ invariant mass spectrum from Ref. [61]. The curves are from coupled channel models, Ref. [70].

$\Lambda(1405)$ signals from similar ones coming from other baryonic resonances lying in the same mass region and sharing the same decay modes. For instance, the $\Sigma^*(1385)$ decay modes partly overlap the $\Lambda(1405)$ decays. However, a method to discriminate $\Lambda(1405)$'s from other strange baryons exists, which relies on the neutral channel decay modes: the $\Sigma^0\pi^0$ decay channel is forbidden to $\Sigma^*(1385)$'s because of isospin conservation while $\Lambda(1405)$'s cannot decay to $\Lambda\pi^0$. This is summarized in Tab. 2.1. The use of an electromagnetic calorimeter capable of detecting neutral pions as well as neutrons combined with a tracking system capable of tracing charged kaons would then do the job, and make this measurement feasible with the proposed facility.

A study of the $\gamma p \rightarrow \Lambda(1405)K^+$ photo-production reaction was recently presented by the CLAS collaboration. Data regard the $\Lambda(1405)$ decay to the $\Sigma^{\pm,0}\pi^{\mp,0}$ final channels, which are presently being analyzed [62]. First indications do not favour the single pole description. However, the charged channel behavior is opposite to the theoretical expectations, which requires further investigations. According to these results, the presence of the low-mass pole can be questioned and the $\Lambda(1405)$ simply be interpreted as a $\bar{K}N$ bound state. If this picture is correct, the $I=0 \bar{K}N$ system can be considered the constituent brick of kaon-multinucleon aggregates. Their quest is today a topical issue in the field of nuclear physics with strangeness [69, 22]. Other $\Sigma^0\pi^0$ measurements were recently reported by the ANKE experiment [61]. Unfortunately, the data are too sparse to unambiguously accommodate chiral model predictions [70, 71]. Fig. 2.12 shows the best fit to the data together with the range of predictions yielded by coupled-channel models [70]. The

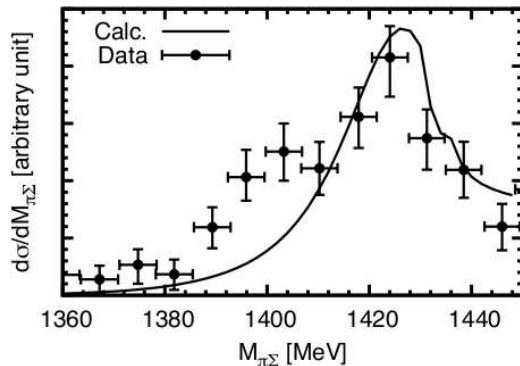


Figure 2.13: $\Sigma\pi$ invariant mass spectrum from the $K^-d \rightarrow \Sigma\pi n$ reaction [66]. The curve is taken from Ref. [71], which relies on a coupled channel approach.

necessity of new quality data remains.

A poorly studied reaction, which might give some meaningful hints on the $\Lambda(1405)$ formation, which can be studied with the proposed experiment is $K^-d \rightarrow \pi\Sigma n$. Its cross section is rather large $\sim 600 \mu\text{b}$ at 600 MeV/ c and $\sim 410 \mu\text{b}$ at 800 MeV/ c . The $K^-d \rightarrow \Lambda(1405)n$ reaction should favor the production of the $\Lambda(1405)$ higher mass pole by means of the $\bar{K}N$ interaction [18]; then, $\Lambda(1405)$'s could be detected via the $\Sigma\pi$ decay channel. The associated neutron, by carrying away the reaction excess energy, might issue useful information on the dynamics of the resonance formation [22]. This channel was measured in past experiments at incident K^- momenta of 686 and 844 MeV/ c [31, 66], and the few existing data agree with the model predictions: they display an enhancement at around 1420 MeV in the $\pi^+\Sigma^-$ mass system. Fig. 2.13 presents the $\pi\Sigma$ invariant mass spectrum [66] along with the model calculations developed in the framework of chiral lagrangians coupled to two channels [71]. The calculations follow the data rather satisfactorily around 1420 MeV/ c^2 , but fail to reproduce the trend at lower invariant masses. New data on this channel would be clearly welcome, especially at lower K^- incident momentum.

Chapter 3

Expected event counting for selected reactions

An assessment of the event counting for the $K^\pm p \rightarrow K^\pm p$ elastic processes is made, which relies on the total cross section values $\sigma_{K^-p} = 80$ mb and $\sigma_{K^+p} = 10$ mb both evaluated at $p_K = 100$ MeV/ c . The event counting is then estimated for an integrated luminosity of 1 fb^{-1} , which is expected to be delivered by DAΦNE in a 2–3 month period. In this time period, the $\phi(1020)$ production cross section ($\sim 3 \mu\text{b}$) is expected to bring about a total of $\approx 3 \times 10^9 \phi$ mesons, or $1.5 \times 10^9 K^\pm$ pairs.

The kaon low momenta call for a thin target, therefore the event counting is only assessed for a gaseous H_2 (D_2) target. The target is required to surround the beam pipe, which is a cylinder of 4–5 cm in diameter coaxial to the e^\pm beams. Such an arrangement requires a target of cylindrical geometry whose inner radius must be capable of accommodating the first two layers of a vertex detector. Such layers are used for tracking the incoming kaons, which are emitted with a $\sin^2 \theta$ angular law from the ϕ decay vertices. The assessment of the number of events arising from elastic scattering measurements ($N_{K^\pm p}$) is made by setting the following parameters

1. the target geometry covers about 70% of 4π (from simulations);
2. about 20% of the incoming kaons decay before reaching the target region (from simulations);
3. the total tracking efficiency of the reaction products is at least 30% (a figure of merit deduced from the FINUDA tracking).
4. multiple scattering and energy loss of kaons crossing the central region media are properly taken into account (by the simulation code).

For a gaseous Hydrogen target operated at 2-3 bar, 2.5 cm thick, 10 cm long and with an inner radius of 6.3 cm, the expected yields are $N_{K^-p} \simeq 3200$ and $N_{K^+p} \simeq 400$ events to be eventually shared between two (possibly three) momentum bins. When assuming a signal to noise ratio as low as 1 and requiring a 7%/bin statistical error for the measured K^+p differential cross section, a complete study requires an integrated luminosity of about 3 fb^{-1} per target. That is, an amount of ≤ 9 months of data taking is necessary to study the Kp elastic scattering at two (possibly three) momenta. An equivalent amount of time is further required for the Kd studies.

In this regard, an assessment for the $\Lambda(1405)$ event counting is made, which uses the $K^-d \rightarrow \Lambda(1405)n$ reaction. Three fb^{-1} will populate the $\Lambda(1405)$ peak with about 200 events. It is worth noting that the $K^-d \rightarrow \Lambda(1405)n$ measurement is a kinematically complete measurement. In conclusion, 3 fb^{-1} per target seems to be a reasonable integrated luminosity to experimentally survey the reactions above discussed with good precision and accuracy.

Chapter 4

Reaction kinematics and experimental constraints

The crab-waist configuration of DAΦNE makes the crossing angle between the e^+e^- beams to span 25 mrad, which causes a ϕ momentum spread of about 15 MeV/c. Accordingly, the decay kaons are emitted with a momentum spread which ranges between 115 and 141 MeV/c as shown in Fig. 4.1. These kaons may induce reactions; occasionally, one of the reaction final par-

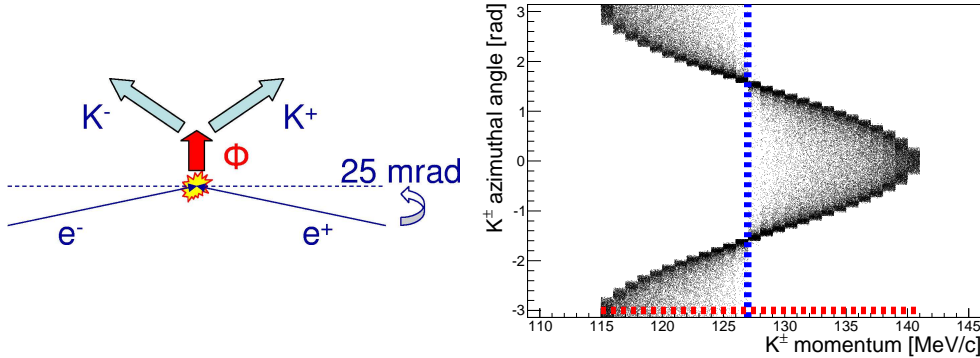


Figure 4.1: Simulated momentum distribution of charged kaons vs their azimuthal angles (right). Kaons are produced by $\phi(1020)$ meson decays which, in turn, are produced by e^+e^- collisions with an electron/positron crossing angle of 25° mrad (left). The red dotted line indicates the maximum momentum spread of kaons, the blue dotted line denotes the kaon momentum for $\phi(1020)$ mesons decaying at rest.

ticles is not detected because of the finite acceptance of the experimental apparatus. However, some of these partially-detected reactions can fully be recovered via the reaction kinematics.

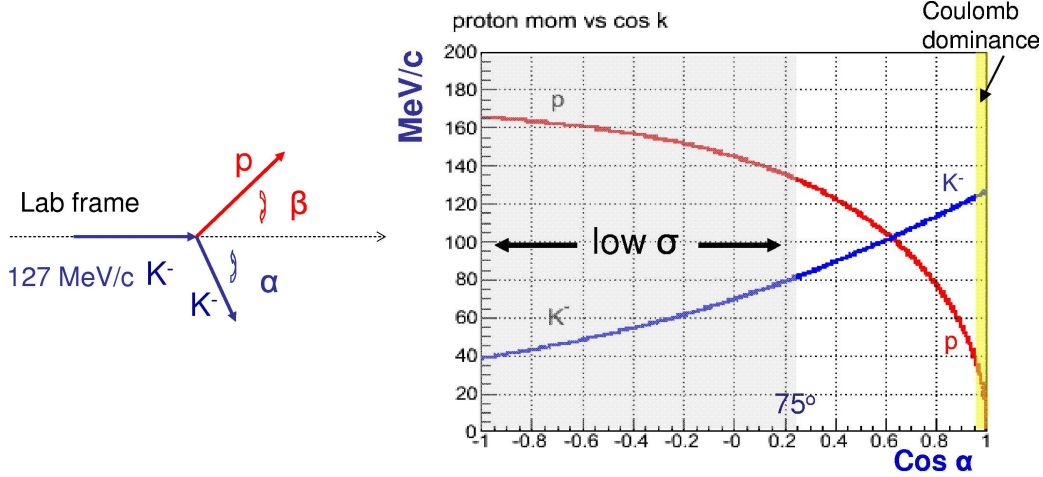


Figure 4.2: Kinematics of the K^-p elastic scattering for an incident momentum of $127 \text{ MeV}/c$. The blue curve shows the momentum of the emitted kaon vs the cosine of the angle between the kaon direction and the beam direction. The red curve shows the kinematics of the associated proton. More details are given in the text.

As an example, consider the $K^-p \rightarrow K^-p$ elastic scattering with a $127 \text{ MeV}/c$ incident kaon. The momenta of the scattered kaon range from ~ 40 to $127 \text{ MeV}/c$ and the proton momenta can be as high as $\sim 165 \text{ MeV}/c$ as shown in Fig.4.2. This figure also shows that kaons (blue line) of momenta larger than $100 \text{ MeV}/c$ are emitted at forward angles along with protons whose momenta are slower than $100 \text{ MeV}/c$. These protons are hardly detectable; therefore, the reaction is only identified by the kaon detection. For the K^-p elastic scattering, the relevant measurements are performed at angles below 75° , where the reaction kinematics grants the emission of kaons with momenta above $80 \text{ MeV}/c$, which can be tracked by the vertex detector (see next section).

Fig.4.3 presents simulation of the kaon momentum distributions. This simulation accounts for the finite size of VDET, the material budget crossed by kaons and their decays, the crab-waist configuration of DAΦNE and the effects of multiple scattering and energy loss of kaons. Finally, ϕ -mesons are assumed to decay according to a $\sin^2 \theta$ angular law. The distributions represent the momentum shape at the target (Grey filled histogram) and at the outer layer of the vertex detector (VDET, described in the next section). The kaon momenta at the target span the interval $93\text{--}132 \text{ MeV}/c$, which allow studies at two (possibly three) kaon momenta. For the proposed configuration target-VDET, simulation reveals that 75% of the produced kaons

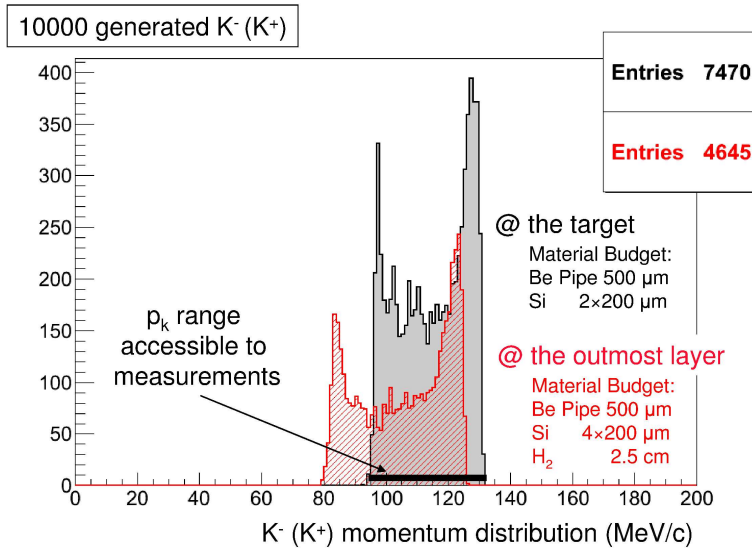


Figure 4.3: Momentum distributions of kaons entering the target (Grey filled diagram) and the outermost layer of VDET. The distributions are the result of simulations, see the text for more details.

impinge on the target.

Chapter 5

The vertex detector (VDET)

The above discussion on the IKON project calls for a vertex detector which must embody the following properties:

1. be finely segmented for a reliable tracking of K^+K^- pairs up to the target and beyond it for kaon elastic scattering measurements;
2. be thin to minimize the kaon energy loss and multiple scattering;
3. capable of mass-identify particles (ex., via dE/dX);
4. capable of operating inside a magnetic field (i.e., the KLOE field $B=0.6T$);
5. capable of delivering a fast trigger when impinged on by pairs of K^+K^- traveling in opposite direction.

The VDET configuration presented in the following responds to requirements 1. throughout 5. However, the final configuration will further rely on R&D as well as on VDET & KLOE joint simulations. R&D will begin upon INFN funding.

5.1 VDET, simulations

The VDET simulations aim at addressing the issues 1. throughout 5., with the VDET being constrained to fit into the free volume between the DAΦNE beam-pipe and the KLOE drift chamber. In the present study only the elastic scattering process $K^\pm N(D) \rightarrow K^\pm N(D)$ is examined since its detection involves only the VDET. The joint role of KLOE & VDET becomes indispensable when studies are directed to all the reaction channels induced by low-energy kaons; namely, the reaction channels described in the Introduction and listed from 1. throughout 7. The simulations are based on GEANT4.

In this simulation it is assumed that the phase space volume of ϕ mesons is populated according to the recently proposed scheme of crab-waist collisions for DAΦNE, that charged particles undergo multiple scattering throughout VDET, and that the interaction of charged particles with the VDET media results only in energy loss for ionization. Finally, particles are assumed to move inside a magnetic field of $B=0.6$ T.

A possible configuration of the IKON vertex detector is sketched in Fig. 5.1. It bears a cylindrical geometry along the Z-axis, which matches the DAΦNE e^+e^- beam directions. The inner layer is the beam-pipe, a beryllium foil 4–5 cm in diameter and 350 μm thick. The beam-pipe layer is followed

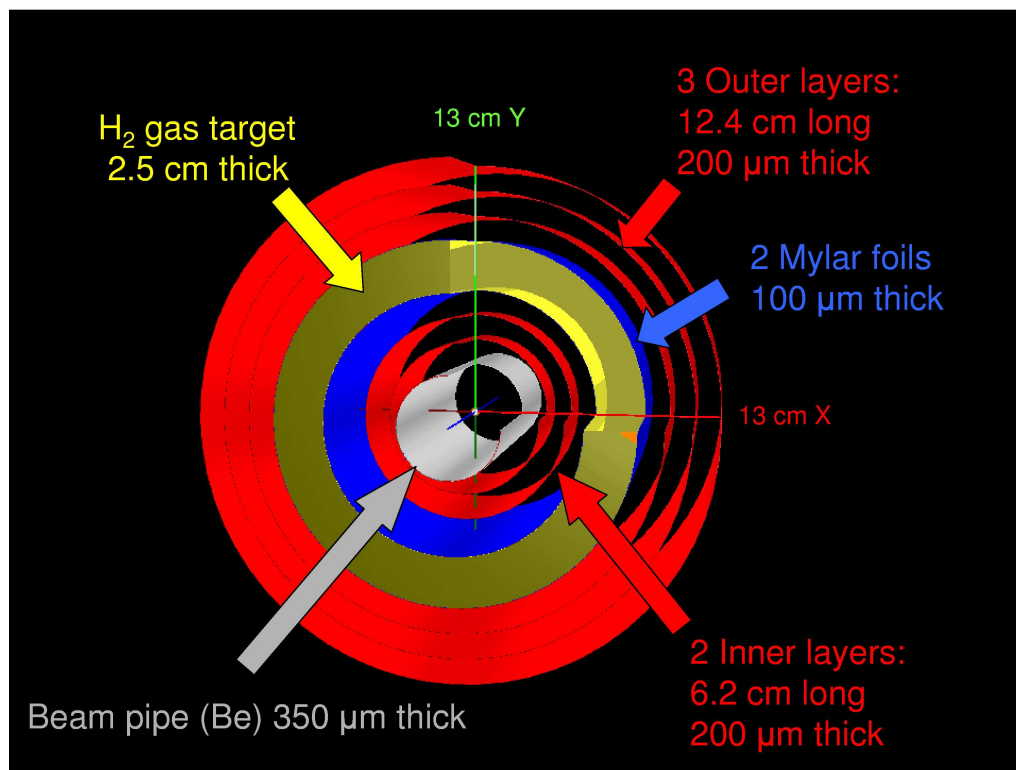


Figure 5.1: A possible configuration of the IKON vertex detector. The Z-axis (in blue) indicates the e^+ and e^- beam axes. In sand is reported the beam-pipe, a beryllium foil 4–5 cm in diameter and 350 μm thick. Two layers of double-sided micro-strip silicon detector (in red) come after. In yellow is the room occupied by a 2.5 atm gas target, which is enclosed with two foils of mylar 100 μm thick (in blue). The target is followed by 3 layers of silicon detector (in red). The maximum occupancy of VDET is also reported.

by two double-sided micro-strip silicon detectors (in red), each 200 μm thick.

The target region comes after, which occupies the volume in yellow, which is 2.5 cm thick. The target is enclosed with two walls (in blue), the walls being foils of mylar 100 μm thick. For this simulation, the target is filled with Hydrogen gas at 2.5 atm. The layers beyond the target region are three 200 μm thick double-sided micro-strip silicon detectors. The inter-layer distance is on the average 1 cm. The first two silicon layers are used for tracking the $\phi \rightarrow K^+K^-$ kaons, while the three outer layers are for reconstructing the trajectories of the elastic scattered kaons or secondary vertices.

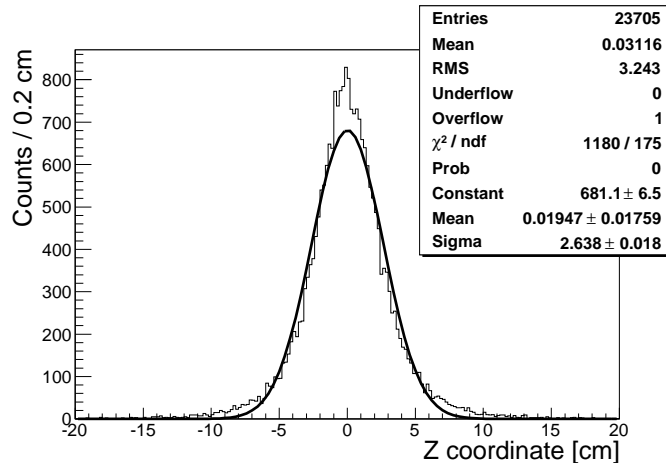


Figure 5.2: Distribution of the coordinates along the VDET Z-axes of the $\Phi \rightarrow K^+K^-$ kaons at the first silicon layer.

The VDET size along the Z-axes is mainly determined by the shape of the $\phi \rightarrow K^+K^-$ kaons distribution. Fig. 5.2 shows this distribution right outside the beam-pipe (first silicon layer), which indicates that a ± 3.25 cm long silicon detector will accept about 80% of the incoming K^\pm beams. The same distribution but for kaon tracks extended up to the third silicon layer (right outside the target) is reported in Fig. 5.3. In this case, a ± 6.5 cm long layer accepts about 70% of the incoming K^\pm beams. As an example, a ± 6.5 cm long silicon layer can be configured by head-on ordering two 6.5 cm long detectors; such a configuration minimizes the material budget traversed by the incoming kaons. As a final consideration, it is worthwhile noting that double-sided silicon sensors 200 μm thick and 6.5 cm long arranged into five detection layers represents nowadays the status-of-the-art for a vertex detector.

The momentum distribution of the $\phi \rightarrow K^+K^-$ kaons is shown in Fig. 4.3: the shape and width are determined by the DAΦNE crab-waist scheme of collisions. For kaons entering the beam-pipe, the distribution has a central

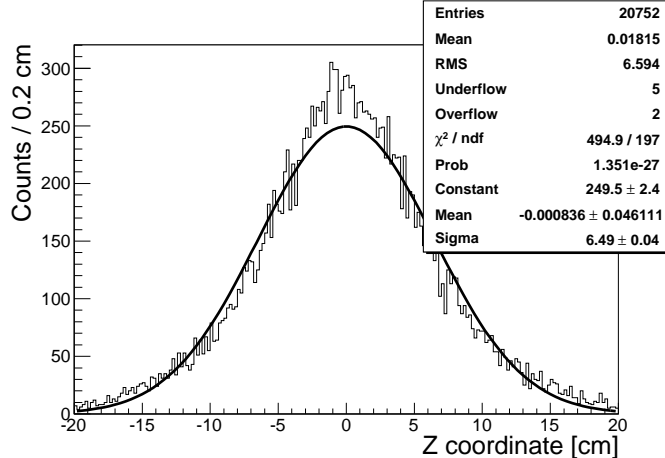


Figure 5.3: Distribution of the coordinates along the VDET Z-axes of the $\phi \rightarrow K^+K^-$ kaons at the third silicon layer (right outside the target).

value of 127 MeV/c and a width of 26 MeV/c (see Fig. 4.1); this layer is indicated as “vacuum” in Tab. 5.1. When kaons traverse the VDET layers the distribution spreads; however, the original shape is substantially kept. The central values and widths of the momentum distributions of kaons entering some VDET layers are listed in Tab. 5.1. The kaon momenta at Si 3rd layer suggests that cross sections can surely be measured at two momentum bins; for instance, at 105 ± 10 and 125 ± 10 MeV/c. Because of the broadening of the kaon momentum distribution (compare the two kaon momentum distributions in Fig.4.3), a further measurement may be carried out at $p_K < 95$ MeV/c. In this case, the decrease of the kaon yield is partially compensated by the general increase of the cross sections (see Figs. 2.2 throughout 2.5). As a final consideration, the GEANT4 simulations of low-momentum charged particles (i.e., $p_K < 95$ MeV/c kaons) interacting with matter (i.e., the VDET media) are fairly imprecise; therefore, unequal to the purpose of learning the behavior of low-momentum kaons in thin silicon

VDET layer	p_K (MeV/c)	Δp_K (MeV/c)
vacuum	127	26
Si 1st layer	121	33
Si 3rd layer	114	38
Si 5th layer	103	45

Table 5.1: Central values and widths of the momentum distributions of $\phi \rightarrow K^+K^-$ kaons entering some VDET layers.

layers. This again calls for bench studies of 200 μm thick double-sided silicon sensors before drawing convincing conclusions.

By following the experience acquired with FINUDA, the VDET silicon layers will also be used to identify the mass of charged particles via dE/dX measurements [22, 23]. Fig. 5.4 shows the result of the simulations for 200 μm thick silicon sensors. In the figure the most probable dE/dX value of MIP's is also indicated (arrow). The comparison makes known that any single layer can mass discriminate kaons from MIPs via particle energy loss measurements. This is a powerful tool to clean spectra from MIPs (ex., Bhabha e^+e^- pairs) as taught by FINUDA, which successfully applied this technique to separate MIPs from kaons, protons, deuterons and tritons [22, 23]. However, such a technique required a major effort when the front-end electronics of the FINUDA silicon sensors was developed; fortunately, this has now become *common practice*.

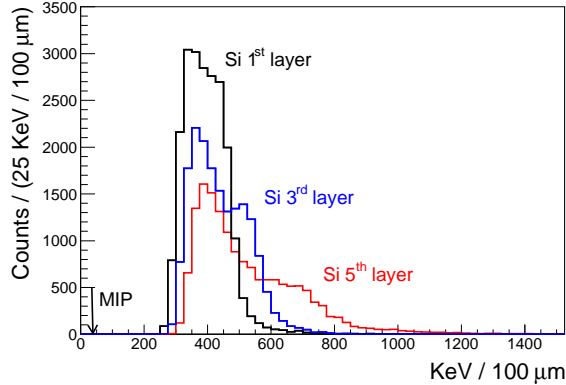


Figure 5.4: Simulations of specific energy loss of $\phi \rightarrow K^+K^-$ kaons at Si first layer (black), Si third layer (blue) and Si fifth layer (red).

It is worth mentioning the simulation outcome of the kaon multiple scattering and its influence on angular distribution measurements. When crossing the VDET media, low-momentum kaons undergo multiple Coulomb scattering, which deflects the original kaon directions. In order to study the effects, a 127 MeV/ c pencil beam of kaons is sent through the beam-pipe/gaseous-target/VDET media and the angular distribution of diffused kaons is studied right outside the VDET fifth layer. At this layer, about 133 mm far from the ϕ production point (see Table 5.2), the angular distribution is described for both the x- and y-coordinate by a Gaussian distribution with $\sigma \sim 1.5^\circ$. That is, differential cross section measurements can well be performed, the uncertainty being 4–5° at full-width half-maximum.

5.2 VDET, hardware

As outlined in the previous section, the physics of IKON constrains the VDET architecture; for instance, VDET is required to have minimal material budget and large dynamic range. As for the former, simulations indicate that the 5 tracking layers should not exceed a total thickness of ~ 1 mm silicon equivalent. The latter constraint requires VDET to be capable of handling particle energy losses in a 1-20 MIP dynamic range to provide reliable PID (see Fig. 5.4). The VDET spatial resolution should be about $100 \mu\text{m}$, any better figure being spoiled by the relevant multiple Coulomb scattering of kaons with the VDET media. At present, some VDET configurations are under scrutiny, the option discussed in this section regards a double-sided micro-strip silicon detector, which is shown in Fig. 5.5. To simplify the VDET construction, it is chosen to build 100 identical Si modules (ref. Table 5.2).

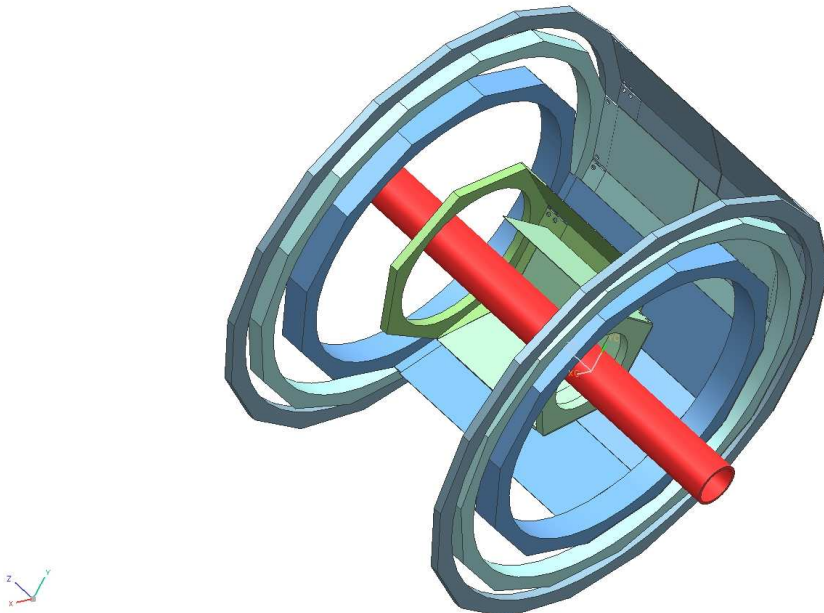


Figure 5.5: Computer-Aided Design (CAD) of VDET. The DAΦNE beam-pipe (in red) is encircled by the VDET supporting mechanics (five layers). The VDET modules are drawn in blue (inner layers) and in green (outer layers).

VDET layer	No.of sensors	Radius (mm)
Si 1st	5	44.7
Si 2nd	7	51.9
Si 3rd	2×12	93.3
Si 4th	2×15	117.0
Si 5th	2×17	133.0

Table 5.2: Characteristics of each VDET layer.

Table 5.2 summarizes the number of sensors populating each VDET layer and the radius of each layer. The size of each sensor is $50 \times 65 \times 0.2 \text{ mm}^3$.

5.2.1 Sensor

Double-sided micro-strip silicon sensors $200 \mu\text{m}$ thick are fabricated on 4" wafers; therefore, no specific R&D is needed [74]. This is an important achievement since the experiment timescale (3-4 years) does not permit long R&D developments. Nowadays, the standard thickness of double-sided micro-strip silicon sensors is $300 \mu\text{m}$. The optimum spatial resolution for the proposed measurements is $\leq 100 \mu\text{m}$ (from simulations), which can be fulfilled with a sensor pitch of $\sim 200 \mu\text{m}$.

Sensors $200 \mu\text{m}$ thick would noticeably improve the VDET performances to $KN(D)$ elastic scattering measurements and clearly loose constraints on the thickness of the other unavoidable VDET layers (i.e., fan-outs, aluminum foils, etc). In order to reduce the sensors cost, the possibility of minimizing the number of lithographic steps will also be evaluated; for instance, by punch-through biasing of sensors.

The VDET simulation uses a continuous cylindrical geometry for all the layers (see Fig. 5.1). The VDET is actually segmented into prisms; for instance, the VDET inner layer is a prism with an pentagonal base, the size of each face being $\sim 50 \times 65 \text{ mm}^2$. Special care is put at minimizing the mass of the detector holder. A carbon-fiber structure is being devised for VDET: sensors are only sustained by thin ribs, while the main mechanical holding structure is placed outside of the sensitive volume.

5.2.2 Read-out Electronics

The read-out electronics should be placed outside the VDET acceptance to avoid increasing material budget. This calls for the use of fan-outs to re-route the short transverse strips towards the VDET short edge. However, fan-outs are themselves part of the VDET material budget. In order to

minimize the fan-outs material ultra-thin *microcables* can be used. Such passive structures were adopted for the Inner Tracking System (SSD-ITS) of the ALICE detector. Microcables consist of ultra-thin aluminum foils (14 μm thick) deposited on 10 μm thick polyamide layers. A similar solution appears to be a reasonable choice for the IKON VDET.

The project timescale does not allow a dedicated read-out chip to be developed; therefore, on-shelf electronics will be utilized. The large dynamic range required by the IKON physics sensibly narrows the available choice of chips; however, both HAL25 (SSD-ITS, ALICE) [72] and VA1 (FINUDA) [73] have a dynamic range sufficient to fulfill the IKON requirements. Also, the option of self-triggering chips is investigated with the aim at further reducing the VDET thickness; in fact, such a solution avoids using *thin* scintillator barrels to generate a trigger for the VDET electronics. The VA1TA option of the VA1 chip is a viable solution. Furthermore, the use of the VA1TA chip implies several advantages in terms of R&D and costs since some proponent members have acquired experience with both VA1 and VA1 equipped devices [73].

As far as the noise behavior is concerned, the S/N value for a 6.5 cm long strip sensor to MIP particles can be estimated to be around 30 for the p-side and 25 for the n-side [74]. This value grows about 10 times when detecting low-momentum kaons (see Fig. 5.4), which allows for a high quality kaon detection and discrimination.

Both the hybrid circuits hosting the read-out chips and other electronic circuits needed to drive the digital signals and to provide the proper power to the electronics have to be designed. For instance, signal buffering is to be made to be able to safely transmit signals outside the magnet over a distance of ~ 4 m, as requested by the configuration of the experimental apparatus.

Bibliography

- [1] Review of particle physics, *Phys. Lett.* **B667** (2008), 1
- [2] DEAR Collaboration, G. Beer *et al.*, *Phys. Rev. Lett.* **94** (2005), 212309
- [3] M. Iwasaki *et al.*, *Phys. Rev. Lett.* **78** (1997), 3067
T.M. Ito *et al.*, *Phys. Rev.* **C58** (1998), 2366
- [4] B. Borasoy, R. Nißler, W. Weise, *Phys. Rev. Lett.* **94** (2005), 213401
Eur. Phys. J. **A25** (2005), 79
- [5] B. Borasoy, R. Nißler, W. Weise, *Phys. Rev. Lett.* **96** (2006), 199201
- [6] B. Borasoy, U.-G. Meißner, R. Nißler, *Phys. Rev.* **C74** (2006), 055201
- [7] A. Cieplý and J. Smejkal, arXiv:0910.18221 (nucl-th)
- [8] J. Révai and N.V. Shevchenko *et al.*, *Phys. Rev.* **C79** (2009), 035202
- [9] N. Kaiser, Siegel, W. Weise, *Nucl. Phys.* **A594** (1995), 325
- [10] D.N. Tovee *et al.*, *Nucl. Phys.* **B33** (1971), 493
R.J. Nowak *et al.*, *Nucl. Phys.* **B139** (1978), 61
- [11] E. Oset, A. Ramos, *Nucl. Phys.* **A635** (1998), 99
- [12] J. A. Oller, U.-G. Meißner, *Phys. Lett.* **B500** (2001), 263
- [13] P. Gensini, in *DAΦNE 91, Workshop on Physics and Detectors for DAΦNE*, pag. 453
P. Gensini, in *The Second DAΦNE Physics Handbook* (1995), pag.
R.C. Barrett, in *DAΦNE 91, Workshop on Physics and Detectors for DAΦNE*, pag. 465 P. Gensini, arXiv:0603043v2 (nucl-th)
- [14] A. Olin, T.S. Park, *Nucl. Phys.* **A691** (2001), 295c

- [15] N. Kaiser *et al.*, *Nucl. Phys.* **A612** (1997), 297
 J. Caro Ramon *et al.*, *Nucl. Phys.* **A672** (2000), 249
 M.F.M. Lutz and A. Kolomeitsev, *Nucl. Phys.* **A700** (2002), 193
- [16] L. Roca *et al.*, *Phys. Rev.* **C78** (2006), 025206
 L. Roca *et al.*, *Proceedings of the HADRON05 Conference*, AIP Conference Proceedings **814** (2006), pag. 266
 M. Kaskulov and E. Oset, *Phys. Rev.* **C73** (2006), 045213
- [17] W. Weise and R. Härtle, *Nucl. Phys.* **A804** (2008), 173
- [18] D. Jido, E. Oset and T. Sekihara, arXiv:0904.3410v2 (nucl-th)
- [19] J. Esmaili, Y. Akaishi, T. Yamazaki, arXiv:0906.0505v1 (nucl-th)
- [20] C. Vander Velde-Wilcquet *et al.*, *Nuovo Cim.* **A39** (1977), 538
 P.A. Katz *et al.*, *Phys. Rev.* **D1** (1970), 1267
- [21] FINUDA Collaboration, M. Agnello *et al.*, *Phys. Rev. Lett.* **94** (2005), 212303
 S. Piano, *Proceedings of the Sendai International Symposium on Strangeness and Hadronic Systems SENDAI08*
- [22] FINUDA Collaboration, M. Agnello *et al.*, *Phys. Lett.* **B654** (2007), 80
 FINUDA Collaboration, M. Agnello *et al.*, *Eur. Phys. J.* **A33** (2007), 283
- [23] FINUDA Collaboration, M. Agnello *et al.*, *Phys. Lett.* **B669** (2008), 229
- [24] FINUDA Collaboration, M. Agnello *et al.*, *Phys. Lett.* **B649** (2007), 25
- [25] C.B. Dover and G.E. Walker, *Phys. Rev.* **89** (1982), 1
- [26] S. Eidelman *et al.*, *Phys. Lett.* **B592** (2004), 1
- [27] T. Bowen *et al.*, *Phys. Rev.* **D2** (1970), 2599
 T. Bowen *et al.*, *Phys. Rev.* **D7** (1973), 22
- [28] A.S. Carroll *et al.*, *Phys. Lett.* **B45** (1973), 531
- [29] M. Hoffmann *et al.*, *Nucl. Phys.* **A593** (1995), 341
- [30] A. Sibirtsev *et al.*, *J. Phys.* **G32** (2006), R395

- [31] C.J. Adams *et al.*, *Nucl. Phys.* **B66** (1973), 36
- [32] W. Cameron *et al.*, *Nucl. Phys.***B 78** (1974), 93
- [33] A. Olin, in *Physics and Detectors for DAΦNE*, *Frascati Phys. Series* **16** (1999), 627
- [34] J. Gasser, H. Leutwyler, M.E. Sainio, *Phys. Lett.* **B253** (1991), 252
 J. Gasser, H. Leutwyler, M.E. Sainio, *Phys. Lett.* **B253** (1991), 260
 J. Gasser, H. Leutwyler, *Phys. Rep.* **C87** (1982), 77
 J. Gasser, H. Leutwyler, M.P. Locher, M.E. Sainio, *Phys. Lett.* **213B** (1988), 85
 J. Gasser, M.E. Sainio, A. Svarc, *Nucl. Phys.* **B307** (1988), 779
- [35] W. Kluge, in *DAΦNE 91, Workshop on Physics and Detectors for DAΦNE*, pag. 469
 J. Gasser *et al.*, in *Physics and Detectors for DAΦNE*, *Frascati Phys. Series* **16** (1999), pag. 659
- [36] R.L. Jaffe and C.L. Korpa, *Comm. Nucl. Part. Phys.* **17** (1987), 163
- [37] P. Gensini, *Nuovo Cim.* **60A** (1980), 221
 P. Gensini, *Nucl. Phys.* **7** (1981), 1177
 P. Gensini, *Nuovo Cim.* **102A** (1989), 75
- [38] D. Bugg *et al.*, *Phys. Rev.* **168** (1968), 1466
- [39] R. Krauss *et al.*, *Phys. Rev.* **C46** (1994), 2569
- [40] G. Giacomelli *et al.*, *Nucl. Phys.* **B42** (1972), 437
- [41] C.J.S. Damerell *et al.*, *Nucl. Phys.* **B94** (1975), 374
- [42] W. Slater *et al.*, *Phys. Rev. Lett.* **7** (1961), 378
- [43] R.J. Glauber, *Phys. Rev.* **100** (1955), 242
 V. Franco and R.J. Glauber, *Phys. Rev.* **142** (1966), 1195
- [44] R.G. Glasser *et al.*, *Phys. Rev.* **D15** (1977), 1200
- [45] G. Giacomelli *et al.*, *Nucl. Phys.***78** (1974), 285
- [46] M. Sakitt *et al.*, *Phys. Rev.* **139** (1965), 719
- [47] W.E. Humphrey and R.R. Ross, *Phys. Rev.* **127** (1962), 1305

- [48] J.K. Kim, *Phys. Rev. Lett.* **21** (1965), 29
- [49] W. Kittel *et al.*, *Phys. Lett.* **21** (1966), 349
- [50] J. Ciborowski *et al.*, *J. Phys.* **G8** (1982), 13
- [51] D. Evans *et al.*, *J. Phys.* **G9** (1983), 885
- [52] R. Armenteros *et al.*, *Nucl. Phys.* **B18** (1970), 425
- [53] A. Deloff, *Nuovo Cim.* **102A** (1989), 217
- [54] O. Dahl *et al.*, *Phys. Rev. Lett.* **6** (1961), 142
T.H. Tan, *Phys. Rev. Lett.* **23** (1969), 395; *Phys. Rev.* **D7** (1973), 600
- [55] O. Braun *et al.*, *Nucl. Phys.* **B124** (1977), 45
- [56] D. Cline *et al.*, *Phys. Rev. Lett.* **20** (1968), 452
D. Eastwood *et al.*, *Phys. Rev.* **D3** (1971), 2603
D.P. Goyal *et al.*, *Phys. Rev.* **D18** (1978), 948
- [57] G. Bendiscioli *et al.*, *Nucl. Phys.* **A789** (2007), 222
G. Bendiscioli *et al.*, *Eur. Phys. J.* **A40** (2009), 11
- [58] FINUDA Collaboration, S. Piano, in *Proceedings HYP-X Conference* (Tokai, Japan, 2009), in press
- [59] FOPI Collaboration, N. Herrmann, in *Proceedings of the EXA05 Conference*, Austrian Academy of Science Press (2005), ISBN 3-7001-3616-1, p. 73
- [60] A. Barbaro-Galtieri *et al.*, *Phys. Lett.* **5** (1963), 63
M. Niiyama *et al.*, *Phys. Rev.* **C78** (2008), 035202
- [61] I. Zychor *et al.*, *Phys. Lett.* **B660** (2008), 167
- [62] CLAS Collaboration, K. Moriya and R. Schumacher, in *Proceedings of the HYP-X Conference* (Tokai, Japan, 2009), in press: arXiv:0911.2705v1 (nucl-ex)
- [63] T. Hyodo, W. Weise, *Phys. Rev.* **C77** (2008), 035204
- [64] E. Oset, A. Ramos, C. Bennhold, *Phys. Lett.* **B527** (2002), 99
- [65] T. Hyodo, S. Nam, D. Jido, A. Hasaka, *Phys. Rev.* **C68** (2004), 018201
- [66] O. Braun *et al.*, *Nucl. Phys.* **B129** (1977), 1

- [67] R. J. Hemingway, *Nucl. Phys.* **B253** (1985), 742
- [68] R.H. Dalitz and A. Deloff, *J. Phys.* **G17** (1991), 289
- [69] M. Agnello *et al.*, *Phys. Rev. Lett.* **94** (2005), 212303
- [70] R. Nißler, PhD thesis, 2008
- [71] L.S. Geng, E. Oset, *Eur. Phys. J.* **A34** (2007), 405
- [72] F. Agnese *et al.*, *Nucl. Instr. and Meth.* **A562** (2006), 110
- [73] P. Bottan *et al.*, *Nucl. Instr. and Meth.* **A427** (1999), 423
- [74] One of the authors (Luciano Bosisio) has already studied the response of 200 μm thick double-sided micro-strip silicon detectors to MIPs.